



Soft gallstone-crushing robots

Lin Xu^{1,5,†}, Heting Wu^{1,2,†}, Weiqi Qian^{1,2}, Yang Wang¹, Chris R. Bowen³,
Zhong Lin Wang^{1,4,*}, Ya Yang^{1,2,5,*}

¹ CAS Center for Excellence in Nanoscience, Beijing Key Laboratory of Micro-nano Energy and Sensor, Beijing Institute of Nanoenergy and Nanosystems, Chinese Academy of Sciences, Beijing 101400, PR China

² School of Nanoscience and Technology, University of Chinese Academy of Sciences, Beijing 100049, PR China

³ Department of Mechanical Engineering, University of Bath, BA27AK, UK

⁴ School of Material Science and Engineering, Georgia Institute of Technology, Atlanta, GA 30332-0245, USA

⁵ Center on Nanoenergy Research, School of Physical Science and Technology, Guangxi University, Nanning 530004, PR China

The current treatment for symptomatic gallstones is primarily surgical, where one of the most general surgeries, laparoscopic cholecystectomy, is the excision of the gallbladder to remove gallstones. However, postoperative site infections are a common health risk. As a result, scientists are investigating non-invasive methods to crush gallstones, but to date there are limited reports on such approaches. Herein, we propose a non-invasive lithotripsy method that uses ferromagnetic, spiny, flexible, and wireless medical robots, that can be taken orally into the human body bio-safely, to achieve efficient crushing of human gallstones. After operating for 30 minutes, a human gallstone of about 1 cm in diameter had been crushed into a pile of powdered gallstone residue by three soft gallstone-crushing robots in a pig gallbladder. The work highlights that our designed soft robot provides a promising pathway for non-invasive treatment of human gallstones disease, which brings new insights for future advancement of soft medical robots.

Keywords: Ferromagnetic; Flexible composite materials; Medical robot; Gallstone crushing; Noninvasive treatment

Introduction

The gallbladder is a vital digestive organ of the human body. It not only can store, concentrate and excrete bile, but also plays an essential role in regulating biliary pressure inside and outside the liver and aiding secretion and immunity [1–3]. When gallbladder stones are formed (cholelithiasis), they act to stimulate the gallbladder mucous membrane and induce chronic and acute inflammation of the gallbladder. Long-term stimulation of the gallbladder mucosa by these stones can lead to gallbladder cancer. Currently, the conventional treatment for cholelithiasis is a surgical procedure to directly remove the gallbladder [4–7].

However, clinical studies have revealed that there are clear indications and risks associated with such surgery. In general, the gallbladder is the main production site for intestinal immunoglobulin, and the gallbladder mucosa is responsible for secreting Immunoglobulin A antibodies, which plays an essential role in the immune system. As a result, the gallbladder is the primary organ with protective antibodies, which is important for the immune defense of the biliary system. Consequently, the loss of vesicular function following cholecystectomy increases the risk of colorectal cancer [8]. Therefore, cholelithiasis treatment without the removal of the gallbladder is a preferred approach for human health.

To date, researchers have put forward a range of minimally invasive operations. One approach is to view the interior of the

* Corresponding authors.

E-mail addresses: Wang, Z.L. (zhong.wang@mse.gatech.edu), Yang, Y. (yayang@binn.cas.cn).

† Both authors contributed equally to this work.

gallbladder with a choledochoscope and the periphery of the gallbladder with a laparoscope, both preoperatively and intraoperatively, and using a combined two-scope approach to operate from the inside out [1]. The whole procedure is minimally invasive, visible and safe, and does not lead to complete removal of the gallbladder, allowing the patient to gain a higher degree of benefits. However, the costs of the procedure are high and the standards for patient selection are strict. Another promising method relies on an extracorporeal lithotripter to generate a shock wave that is focused on the stone to release energy over a number of cycles to shatter the stone in the body [9,10]. This is a relatively safe and effective procedure, with minimal postoperative side effects after surgery. As with cholecystectomy gallstone removal, the cumbersome nature of this technique, its range of potential contraindications (pregnancy, coagulopathy), and its selective selection of patients have prevented its widespread adoption [8]. Therefore, there is a need for further research on the development of a gallstone removal treatment with a specific focus on non-invasion, bio-safety, convenience and high efficiency (Supplementary Table S1).

In recent years, soft medical robots have been reported that enable drug delivery [11], diagnosis [12], surgery [13], rehabilitation [14], therapy and use as auxiliary tools [15–18]. With the benefits of efficiency, accuracy, repeatability, reliability and cost-effectiveness, micro-medical robots have had a far-reaching impact on the future of medicine [13,16,19–26]. In this work, we propose the first magnetically controlled, battery-free, flexible, prickly miniature medical robot that can realize efficient crushing of human gallstones by a noninvasive lithotripsy method. The robot is made of ferromagnetic powder and flexible silicone rubber materials with good biocompatibility. The spiny spherical structure allows the robot to travel through the digestive system, and also increases the contact pressure when it collides with a gallstone. The soft robot can be under the control of an applied magnetic field, and has potential to move through the oral cavity, esophagus, stomach, duodenum, common bile duct and cystic duct into the gallbladder. The application of a pulsed magnetic field leads to periodic vibration of the robot in the gallbladder to enable direct contact with gallstones via collisions. This approach establishes a noninvasive, highly efficient and safe means of crushing human gallstones, with wide application potential (Fig. 1a–d and Supplementary Video S1). The elaborate design of the robot was carefully considered: the use of ferromagnetic materials allows the robot to be actuated successfully by pulsed magnetism to rapidly crush human gallstones; the soft, multi-spiked skin of the robot facilitates collision with gallstones and reduces the contact area and sliding friction with the digestive tract. The consequences of the soft medical robot with this innovative lithotripsy technology will be far-reaching, which involves application fields that are not confined to lithiasis (gallstones), but also can be extended to eliminate blood clots, dredge blood vessels and increase gastric motility.

Results and discussion

Spiny skin for the robot

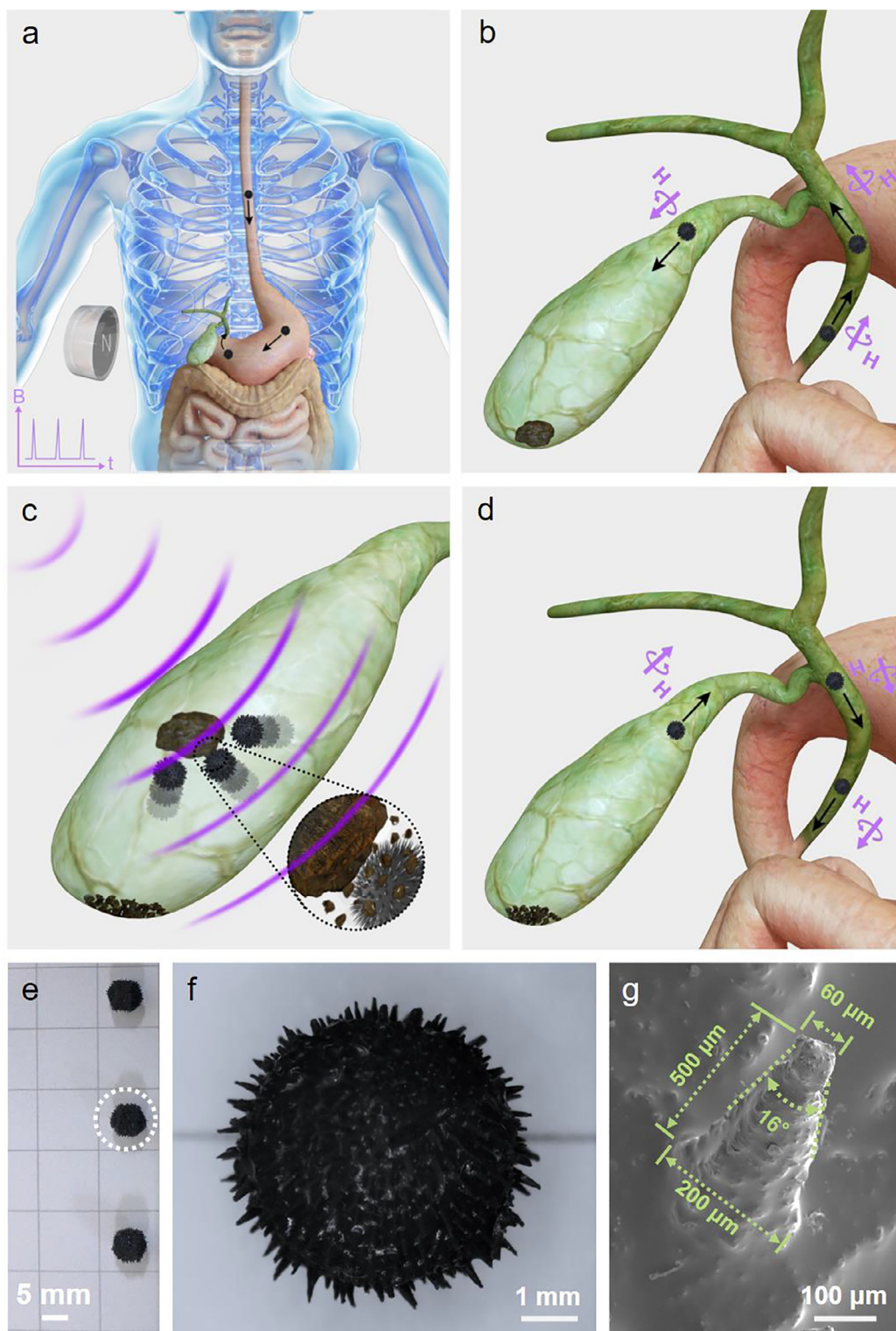
For the robot to be able to enter the gallbladder freely and crush gallstones efficiently, it is necessary to incorporate a flexible skin

with a multi-spine structure on the surface of the spherical magnetic core of the robot. The spiny skin of the functional layer is prepared by a one-step magnetic powder-assisted molding approach consisting of a polydimethylsiloxane (PDMS) matrix that is uniformly mixed with iron powder (Supplementary Fig. S1a). The high density and long spines of the structure prevents the robot from sticking to the inner wall of the intestine. To ensure that long spines are obtained with a maximum density of spines, the particle size of the iron powder and the mass ratio of hexane, which acts as a dispersing agent for the iron powder, were investigated to design the optimal multi-spine robotic skin composition (Supplementary Fig. S2a–f). The obtained optimized multi-spine skin (Supplementary Fig. S2g) exhibits a spiny structure that resembles a cone with a slightly blunt tip (top angle of 16 degrees and bottom diameter of 200 μm). The area of the distributed spiny protruding structures (total S_i) is approximately 50% of the whole skin, and the average length of the spines L_i is 500 μm , as shown in Supplementary Fig. S1b, c, Supplementary Fig. S2e, and Fig. 1g.

Spherical ferromagnetic robots (Fig. 1e, f) possessing a dense distribution of spines of the skin have long-term implantable bio-compatibility and flexibility. The multi-spine skin operates as a physically tough and functional robotic coating that prevents adhesion to the skin of the digestive tract and increases the pressure associated with contact collisions with human gallstones, with strain-limiting mechanics to prevent damage to the ferromagnetic functional material. The robot resides inside the body during the entire treatment and when the treatment is completed, the robot will be directed out of the body by a controlled magnet.

Movement characteristics of gallstone-crushing robot

The dynamic motion of the robot is primarily controlled by a pulsed magnetic field. Due to the presence of iron powder in the robot, it can perform periodic movements in response to an applied periodic pulsed magnetic field (≤ 0.3 T) that is emitted by a medical pulsed magnetic therapy instrument. To reveal the underlying mechanism of the intriguing degree of motion exhibited by our multi-spine robot, we analyzed the periodic, and successive motions of a single robot in a gallbladder model. Moreover, its dynamics have been simulated by multi-physics field modelling. The designed transparent gallbladder model was 3D printed according to the human gallbladder at a 1:1 scale. The forces acting on the ferromagnetic robot in response to the dynamic magnetic field and its gravity principally determine its kinematic properties in the gallbladder model. Since 90% of the bile stored in the gallbladder is water, its viscosity and density are similar to water. Therefore, we filled the gallbladder model with water to simulate the liquid conditions in the gallbladder and facilitate our observation and high-speed photographic analysis of the robot's movement in the transparent gallbladder model. There are two main robot locomotion types: parabolic (Fig. 2a) and sliding (Fig. 2b). The cause of these different patterns (Supplementary Figs. S3 and S4) is related to the different robot locations, and associated magnetic field strengths, during the start and fall of the individual cycle movements (Supplementary Video S2). The position of the pulsed magnetic field was fixed during testing and observation, therefore the intensity

**FIGURE 1**

An overview of the soft gallstone-crushing robots and the lithotripsy mechanism. (a–d) Overview of the properties and application of the robots. (e) Optical images of the assembled robots. A magnified, detailed view of the robot's appearance is also shown in the image (f). Average diameter of the spherical robot is 5 mm. (g) SEM image of a single spine.

of the magnetic field varied from position to position in the gallbladder model (Supplementary Figs. S5–S7), and the force of attraction of the magnetic field on the robot differs from position to position. As shown in Fig. 2c, at Position 1 the magnetic field

is turned on and the robot begins to move in response to the applied magnetic field; at Position 2 the magnetic field is already turned off, at which point the robot begins to fall under gravity until it falls to the bottom of the model, where the cycle ends.

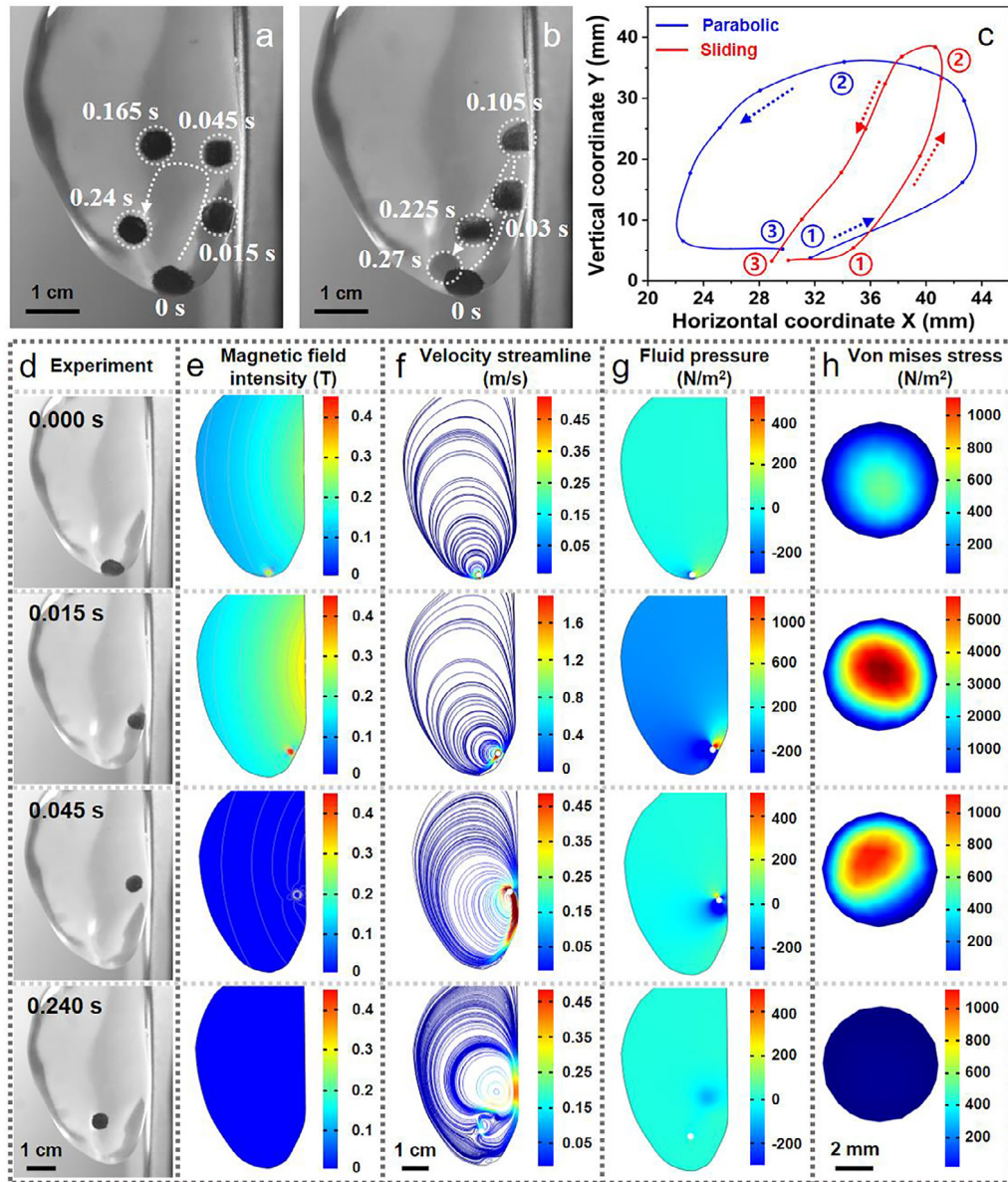


FIGURE 2

Study of the kinetics of ferromagnetic robot and fluid field. (a–c) Diagram of the two main trajectories of the robot in the gallbladder model: parabolic (a, blue line in Fig. 2c) and sliding (b, red line in Fig. 2c). There is only one robot involved in this illustration. (d–h) Experimental and simulated snapshots of the parabolic motion in a single cycle. The time and movement corresponding to each horizontal row is the same.

The robot moves reciprocally as the pulsed magnetic field is periodically switched on and off (at 80 pulses per minute), which leads to the periodic rising and falling. Dimensional calibration and creation of a coordinate system of the robot motion from video images captured by the high-speed camera allows the robot's motion trajectory to be tracked; as a result, its velocity (Supplementary Fig. S8a) and acceleration (Supplementary Fig. S8b) can be calculated. At a magnetic field intensity of 0.3 T and a pulse frequency of 80 times per minute, the maximum movement speed of the robot is approximately 0.8–1 m/s and the maximum acceleration is approximately 50–60 m/s², as shown in Supplementary Fig. S8. The robot's velocity and acceleration data per cycle for different camera viewpoints (per-

pendicular and parallel to the magnetic field), different magnetic field strengths (0.3 T, 0.15 T and 0.1 T) and different pulse frequencies (20, 30, 40, 50, 60, 70 and 80 times per minute) are presented in Supplementary Fig. S9–S12. These results demonstrate the repeatability and well-executed motion characteristics of the robot at each magnetic pulse, and that the movement velocity and acceleration increases with the intensity of the magnetic field.

Theoretical simulation of robot motion mechanics

In order to better understand the kinematic behavior of the robot and the dynamics of the fluid field in the gallbladder model, we investigated the actuation capabilities of the soft gallstone crush-

ing robots through an accurate and effective theoretical framework based on fluid–solid coupling mechanics, supported by model-based finite element simulations, through experimental and numerical methods. With the aid of the quantitative agreement between simulation results (Fig. 2e–h) and experimental results (Fig. 2d) from the kinetic study shown in [Supplementary Video S5](#), we validated the numerical model, which simulates and predicts the dynamic characteristics of fluid movement and the real-time dynamic stress distribution on the robot during the whole process of the movement of the robot in response to the pulsed magnetic field. The results of the simulation (Fig. 2e–h) are fully consistent with the experimental observations (Fig. 2d).

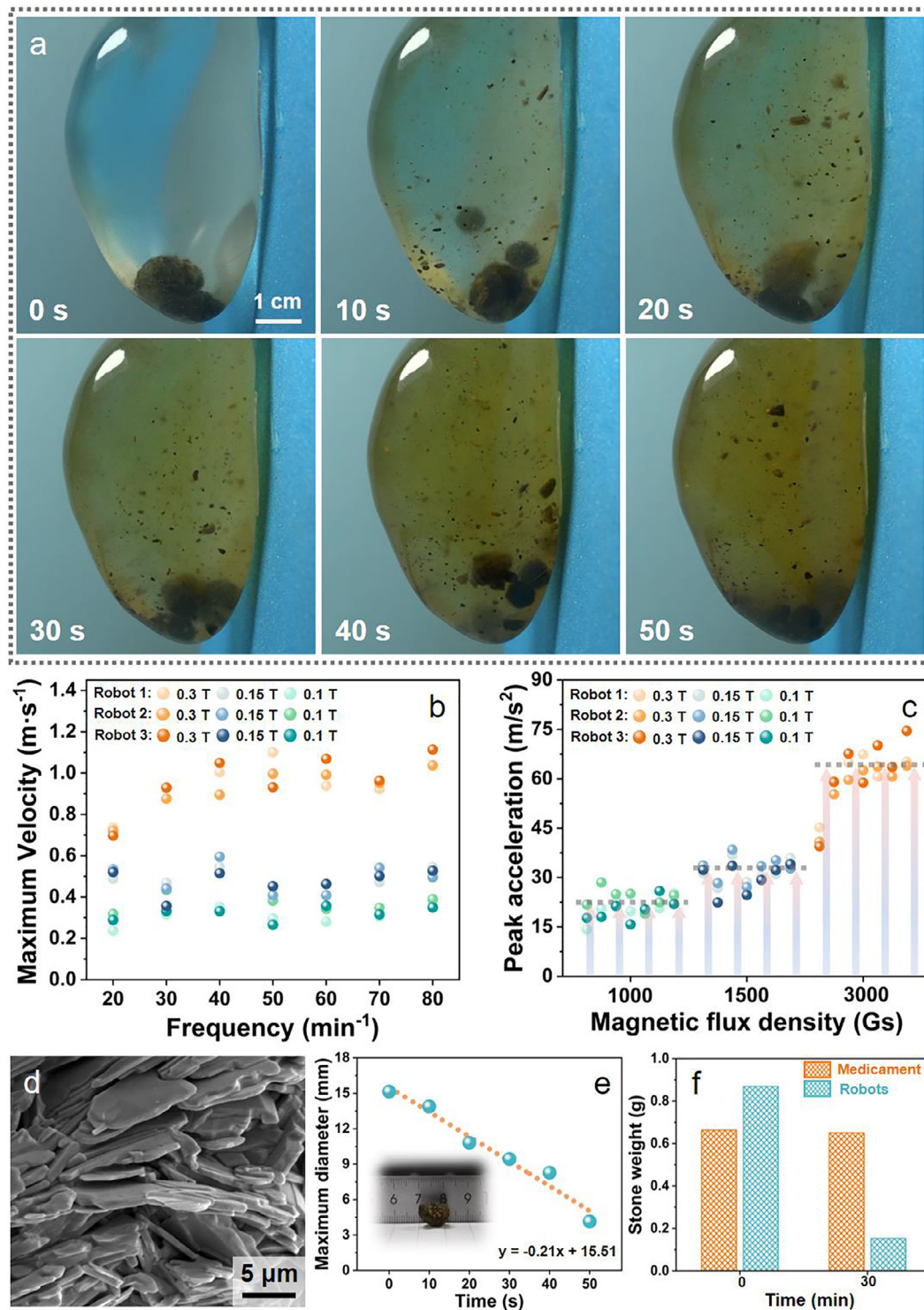
In common with the experiments, the results of the dynamic simulation of the robot revealed that its trajectory resembled a parabola, where the robot reached its highest position at approximately 0.045 s and that one cycle of motion could be completed in 0.24 s. [Fig. 2e](#) demonstrates the calculated magnetic field strength in the model. At 0.015 s, the magnetic field strength reached a maximum value of approximately 0.3 T. According to Newton's law of motion, the acceleration of the robot reached its maximal value at this time, and the fluid velocity in the model is shown in [Fig. 2f](#) and [Supplementary Fig. S13](#). After 0.015 s, the magnet is switched off and the robot falls back to the bottom of the model under the action of gravity and the buoyancy of the liquid (no magnetic attraction). At this stage the robot has completed one cycle of motion and the process begins again. The results from the dynamic simulation of the fluid pressure are presented in [Fig. 2g](#) which enables prediction of the potential fluid pressure to which gallstone may be subjected. When the gallstone is being crushed by the robot, the gallstone will be subjected both a fluid pressure, and the impact force of the robot; the fluid pressure is estimated to be approximately 1000 N/m² at the theoretical maximum fluid pressure ([Fig. 2g](#)). [Fig. 2h](#) reveals the Von Mises Stress of the robot, which indicates that the stresses inside the robot reach their maximum when the robot is subjected to the maximum magnetic attraction. The flexible robot exhibits a different volumetric strain ([Supplementary Fig. S14](#)) due to different external pressures. At 0.015 s, the robot exhibited the maximum volumetric strain, which indicates that the external pressures on the robot also reach the maximum value ([Supplementary Fig. S14](#)). However, this volumetric strain is extremely small (no more than 5×10^{-4}), which has no effect on the function of the soft gallstone-crushing robot.

Experiment on crushing human gallstones

Hereafter, we demonstrated the main capabilities of our gallstone crushing robot, which is designed to be suitable for passage and movement in complex and restricted environments in vivo, such as bile ducts, based on magnetic actuation enabled by a ferromagnetic functional core in the robot's physical body. We envisage that this ferromagnetic robot can be controlled and guided by an external magnetic field to reach the gallbladder in sequence through the mouth, esophagus, cardia, pylorus, duodenum, common bile duct and bile duct to ([Supplementary Fig. S15b, c](#)) perform lithotripsy. For the experimental demonstration, we used a rectangular permanent magnet to apply a guiding control magnetic field to navigate the robot's path of tra-

vel. As we confirmed experimentally ([Supplementary Fig. S15a](#)), the thinnest tube diameter that the robot can pass through is 4.85 mm, which allows it to pass through all the digestive system tubes involved above. We constructed a model diagram of the biliary tract at a scale of 1:1 with the human body ([Supplementary Fig. S15b](#)) and produced a biliary tract model by 3D printing (the smallest bile duct in the biliary system has an internal diameter of 4.9 mm). The same magnet was used to guide the robot from the duodenum, common bile duct and bile duct into the gallbladder. Then, the robot was guided out of the gallbladder and into the intestine ([Supplementary Fig. S15c](#) and [Supplementary Video S4](#)). The experiment confirmed that the robot can freely enter and exit a real human gallbladder through the intestine.

The causes of gallbladder stones are complicated and are attributed to a variety of factors. Any factor that affects the ratio of cholesterol to bile acid concentration or causes bile stagnation can lead to the stone formulation. Human gallbladder stones are a special type of biological crystal. The variable crystalline conditions in the gallbladder do not support the complete development of cholesterol crystals, which form the basic architecture of granular gallbladder stones, and the deposition of amorphous material encourages further stone growth. Scanning electron microscopy of the human gallstones used in our experiments ([Fig. 3d](#)) reveal the structure of their cholesterol sheet sugar-like crystals. To test the potential of the robot to crush a gallstone, we added three robots to the gallbladder model for the lithotripsy operation, and the applied external magnetic field intensity was 0.3 T with a pulsed magnetic field frequency of 80 times per minute ([Fig. 3a](#)). The whole process and results of the mechanical crushing of human gallstone were striking. Within a short period of 50 seconds, the gallstone was broken into a powdery form, while the simulated bile inside the model became cloudy, and the diameter of the largest stone fragment decayed linearly with time, as shown in [Fig. 3e](#), [Supplementary Fig. S16](#) and [Supplementary Video S6](#). A control group of the oral cholelithiasis drug ursodeoxycholic acid and a robotic stone crushing group were established to allow comparison and evaluation of the efficiency that robotic crushing of gallstones can achieve in the treatment of cholelithiasis. The gallstone samples (diameter greater than 1 cm and weight over 0.6 g.) used in both groups were obtained from two intact stones of similar shape and size that were removed by surgery from the same patient ([Supplementary Fig. S17a–d](#)). The simulated bile in the medicament group was a solution of ursodeoxycholic acid and no other treatment was undertaken. The lithotripsy results for both groups are presented in the [Supplementary Fig. S17e–h](#), [Supplementary Fig. S18](#) and [Supplementary Video S7](#). After 30 minutes of magnetic therapy lithotripsy, the gallstone in the robot group had been crushed to fine-grained powder ([Supplementary Fig. S17e](#)), by which the mass of the largest diameter gallstone residue was only ~17.6% of the original stone mass ([Supplementary Fig. S17c, g](#)), while the effect of the drug group was minimal during the same period ([Fig. 3f](#)). What is even more surprising is that all soft robots were undamaged, either in morphology or in mass ([Supplementary Fig. S19](#)). This form of efficient lithotripsy is mainly attributed to the large total effective collision area of the three robots with the gallstone, the large number of robot-gallstone

**FIGURE 3**

Magnetic control strategies for human gallstone-crushing system in a gallbladder model. (a) Snapshots of human gallstone crushing experiment with three robots in a gallbladder model. One photograph was selected at ten-second intervals due to the high efficiency of the crushing stone experiment. (b), (c) Peak velocity (Fig. 3b) and peak acceleration (Fig. 3c) plots for three robots moving at different magnetic field intensities and pulsed frequencies. The higher the intensity of the pulsed magnetic field, the higher the peak velocity and acceleration of its motion. (d) SEM image of a specimen of human gallstone. (e) Curves of the diameter of the gallstone as a function of the duration of the crushing experiment. The functional expression for this linear relationship is $y = -0.21x + 15.51$. (f) Histogram of the change in gallstone weight in the robot and medication (ursodesoxycholic acid) groups.

collisions, and the high velocity more than $1 \text{ m}\cdot\text{s}^{-1}$ (Fig. 3b) and acceleration of up to $75 \text{ m}\cdot\text{s}^{-2}$ (Fig. 3c) of the three robots (Supplementary Video S3).

Robots crushing human gallstone in porcine gallbladder

Unlike the rigid material of the 3D printed gallbladder model, the real gallbladder is soft and flexible. For further verification of the lithotripsy effect of the robot on a real gallbladder, experiments were carried out using a porcine gallbladder (Fig. 4b) instead of the gallbladder model. Using the same approach, we placed three robots (Fig. 4a) with a human gallstone (Fig. 4c and Supplementary Fig. S20a, b) into a water-filled porcine gallbladder (Fig. 4e), and switched on the pulsed magnetic therapy machine (magnetic field intensity of 0.3 T and pulsed magnetic field frequency of 80 times per minute) to undertake the lithotripsy experiment with a video taken throughout the process (Supplementary

Video S8). At 105 s into the experiment, the first fragment was dislodged from the gallstones as the robots oscillated, and then a large number of fragments were dislodged as time progressed and the robots continually collided with the gallstone (Fig. 4e). At approximately 30 min, the gallstone had been crushed into a mass of fragmental residue, as shown in Fig. 4d. In order to avoid the loss of fragments by removing the gallstone debris, which would affect the accuracy of the observations, we performed scanning and imaging via Single Photon Emission Computed Tomography (SPECT) imaging. The SPECT images of the porcine gallbladder, before and after treatment, are presented in Fig. 4f, g, where the gallstone block had been crushed into particulate residues, where the maximum particle diameter of the stone residue was less than 5 mm. The results of the histopathological section shown in Supplementary Fig. S20d, e) also demonstrate the safety of the robolithotripsy approach to the

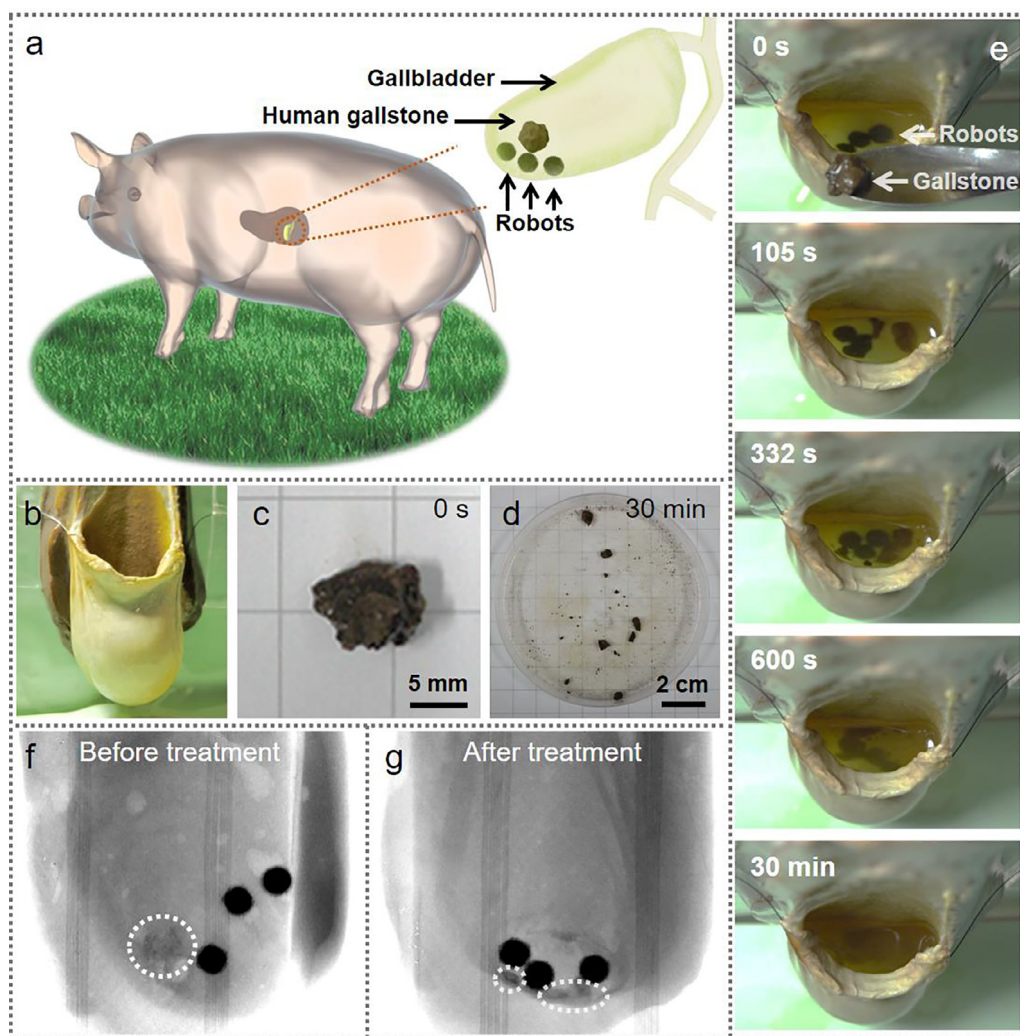


FIGURE 4

Experiments on crushing human gallstone in porcine gallbladder. (a) Schematic of experiment to crush human gallstone in a porcine gallbladder. (b) Optical photograph of a porcine gallbladder used for experimentation and filming the crushing of a human gallstone. The porcine gallbladder is cut with a window (closer to the bile duct) to allow the camera to observe it. (c) Image of human gallstone for this experiment. (d) Photograph of gallstone residue after being crushed. (e) Gallstone crushing. Robots move in displacement under the action of the magnetic field and collide with the gallstone, thereby continuously crushing the gallstone. (f), (g) CT images before and after treatment. The three dark black balls are the gallstone-crushing robots and those indicated by the white dotted boxes are human gallstones. After treatment, a complete block of gallstone (Fig. 4f) turned into a mass of fragmented residue (Fig. 4g). These pictures were obtained via SPECT imaging of an ex-vivo porcine gallbladder.

gallbladder. The histological section of the gallbladder at the site where the robot operated (red boxed area) shows no damage, oedema or loss of the mucosal layer when compared to the site not touched by the robot (green boxed area). The robots can therefore effectively crush human gallstone without any damage to the gallbladder. This is attributed to the fact that both the robots and the gallbladder are soft materials. When a collision occurs, the impact force is weak because of a cushioning effect, and the gallbladder is undamaged (Supplementary Fig. S20d, e). However, since the stiffer human gallstones exhibit a loose lamellar structure with no elastic buffer (Fig. 3d), it is easier for the robots to crush and fragment the gallstone during collisions with robots.

Conclusions

Here, we present millimetre-scale soft multi-spined spherical robots with cyclic motion capability under pulsed magnetic actuation for the non-invasive crushing of human gallstones. Through a theoretical framework based on fluid–solid coupling, supported by our model-based finite element simulations, we have developed a design strategy to investigate the kinematic mechanical properties of a ferromagnetic gallstone crushing robot. The robot's spiny skin on its surface effectively prevents it from adhering to the interior walls of the duct so that it can navigate in complex and constrained environments such as tortuous, sticky-wet and narrow digestive system ducts. By demonstrating the robot's ability to crush gallstones in realistic, clinically relevant *in vitro* environment, we have illustrated the suitability of a soft gallstone crushing robot for potential medical applications.

However, for pre-clinical studies and future clinical translation, further studies will be required to assess the clinical efficacy of the robot and the long-term biocompatibility of our robot. Although these tests were not performed in the current work, there is sufficient evidence that the materials used for the robot may be biocompatible. Firstly, PDMS are known to be biocompatible and have no acute cytotoxicity, which has been reported in a large number of literatures [27–29]. Although no studies have been reported on the cytotoxicity of iron carbonyl powder materials, ISP's iron carbonyl powder has been officially approved by the US Drug Enforcement Administration for direct addition to food as an iron supplement. Also, the use of carbonyl iron powder does not cause toxicity from excessive iron intake [30]. To facilitate the dispersion of the iron powder in PDMS, we used hexane, which is neurotoxic, but its residue is essentially absent from our robots due to the high-temperature of 90 °C experienced in the process of preparation and the total evaporation of hexane. We believe that the proposed soft gallstone crushing robot may be biocompatible and free of acute cytotoxicity; however, further *in vivo* and *in vitro* experimental studies are needed to draw more solid conclusions.

There are several limitations in the current study. Firstly, the robot's movement through the human digestive system as proposed in the conceptual video demonstration (Supplementary Video S1) is achieved with visual feedback, which is challenging to achieve when navigating dynamically and in real time in a human body at a deep level. In practical clinical settings, state

observation is achieved by transillumination imaging (ultrasonography or computed tomography, etc.), which allows for real-time visualization of opaque objects during navigation, so a standard transillumination imaging system would be directly applicable to achieve visual control guidance of the robot in a practical clinical setting, which will be further investigated in prospective research. Movement of the robot in the bile ducts shown in the paper is achieved manually by adjusting the position and orientation of a permanent magnet. In order to improve the accuracy and precision of the robot movement, existing magnetic manipulation guidance systems or full spatial selective magnetic field control [31] will need to be employed to further translate the proposed concept of an *in vivo* soft gallstone crushing robot.

When integrated with these advanced transillumination imaging and full spatial magnetic manipulation techniques, our ferromagnetic multi-spine robot may enable a range of non-invasive or minimally invasive surgical procedures that are currently not possible with existing technologies, not only for the treatment of gallstone disease, but also the removal of blood clots, etc. In summary, the proposed concept of the ferromagnetic multi-spin robot may create new avenues for the non-invasive treatment of gallstones in order to achieve efficient and safe treatment and thus addressing healthcare challenges.

Material and methods

Materials

Commercial PDMS (SYLGARD 184) was acquired from Shanghai Smarttech Co., Ltd. and the percentage of curing agent was 10 wt %. A dispersing agent of n-Hexane (C₆H₁₄) was used to aid dispersion of the carbonyl iron powder (Fe(CO)₅), which was provided by Hebei Zhongye Xindun Co., Ltd. Ursodeoxycholic acid tablets (C₂₄H₄₀O₄) was purchased from Peking University Third Hospital. The pig gallbladder was obtained from the market. The reagents for the preparation of histological section samples, absolute ethanol, xylene, neutral gum were purchased from Sinopharm Chemical Reagent Co., Ltd. The HE (hematoxylin-eosin, HE) staining solution kit was acquired from Wuhan Servicebio Co. Ltd. The human gallstones used in the crushing gallstone experiment were fresh human gallstones from Chongqing General Hospital that were surgically removed with the consent of the patients of laparoscopic cholecystectomy.

Optimization for preparation of soft ferromagnetic spiny skin

For the preparation of robotic spike-like skin, we developed a one-step modified magnetic powder-assisted method [32–35]. Firstly, we fabricated a substrate film by thoroughly mixing PDMS, hexane and iron powder in the mass ratio of 2:1:1 and then coated it on the surface of a hemispherical acrylic spherical shell (45 mm diameter) and cured it by heating at 80 °C for 3 h to form the substrate film. A similar mixture of PDMS, n-hexane and carbonyl iron powder was then evenly applied to the surface of the cured substrate film and a spherical magnet (diameter 30.2 mm, maximum surface magnetic field strength 0.19 T) was placed inside the acrylic spherical shell to form a magnetic spiny film under the influence of the applied magnetic field. Similarly, the material was then cured in a vacuum oven at 80 °C for 3 hours and subsequently peeled off from the hemispherical

acrylic spherical shell to obtain the spiny skin of the robot (Supplementary Fig. S1a).

For optimization of the robot spiny skin composition, we examined a selection of iron particle sizes, mass ratios of iron powder and mass ratios of n-hexane. Carbonyl iron powder with particle sizes of 75 μm , 48 μm , 38 μm , 25 μm , 10 μm , 6.5 μm , 2.6 μm and 1.3 μm were selected to prepare the spiny skin, respectively. The top and side views of the spiny films were photographed with an optical microscope and top view images were analyzed with Image J software. The spiny area of the films was obtained using the following equation to calculate the ratio of the spiny area to the total area:

$$\text{Arearatio} = \frac{\sum_{i=1}^n S_i}{S_T} \quad (1)$$

where S_i denotes the area of individual spine and S_T denotes the total area of the film in the microscope photograph. The area ratio was used to characterize the density of spines on the surface of the film.

The length L_i of each spine in the side view of the film was measured using image processing analysis software and summed to calculate the total length of all spines:

$$\text{Totallength} = \sum_{i=1}^n L_i \quad (2)$$

For optimization of the mass ratio of iron powder (10%–60%) and hexane (5%–45%), we evaluated both the total length of the spines and the ratio of the spiny area in the same way. Based on the experimental results (Supplementary Figs. S2 and S21), a particle size of 6.5 μm for the iron powder and a mass ratio of 2:1:1 for PDMS, n-hexane and carbonyl iron powder were selected for further study.

Fabrication of soft gallstone-crushing robots

There are three main steps in the preparation of the robot: (i) the preparation of the robot spiny skin, (ii) the preparation of the inner core of the magnetic sphere and (iii) assembly of the robot. For the preparation of the inner core of the robot, we mixed PDMS and carbonyl iron powder with a mass ratio of 1:1, and poured it into an acrylic spherical shell mold with a diameter of 5 mm. This was then demoulded after curing, and the inner core of the robot was obtained. To assemble the robot, the obtained spiny film was adhered to the surface of the spherical inner core using PDMS and subsequently cured to create the magnetic spiny spherical robot.

Motion analysis

A 3D printed model of a gallbladder was fixed to the N-pole side of the pulsed magnetic field generator and aligned with the centre of it. A video camera then filmed the robot's motion within the gallbladder model. We used a high-speed camera to capture video of one, two and three robots movement at different magnetic field strengths and pulse frequencies at directions parallel and perpendicular to the magnetic field direction. We tracked and analyzed the robot's motion trajectory from the recorded videos. The horizontal tangent at the bottom of the gallbladder model is taken as the x -axis and the vertical tangent on the left side of the model is regarded as the y -axis to establish the coordi-

nate system. After trajectory tracking analysis, the software automatically measured and calculated the displacement, instantaneous velocity and acceleration of the robots.

Implementation details of simulations

The first step is to construct a simplified simulation of the gallbladder system. We constructed the gallbladder model in COMSOL finite element analysis software (COMSOL Multiphysics 5.4.) to analyse the motion of the robot in the model [36,37]. Since the motion of the robot mainly occurs in the direction perpendicular to the applied magnetic field, we do not consider the motion of the robot in the direction parallel to the magnetic field during the simulation. A two-dimensional model of the gallbladder was built, as shown in Fig. 2d, which served as a solid boundary condition and assumed no slippage in the inner wall of the gallbladder. Since the external spiny structure of the robot occupies a small mass ratio (approximately 10%) and volume ratio (approximately 10%) of the robot, we ignored the spiny structure of the robot skin and modelled the robot as a simple circle to simplify the simulation process. The robot will lead to the liquid flow of bile inside the gallbladder during its motion. We filled the model with turbulence to construct the simulation system of fluid–solid coupling. The material of the robot is assumed to be a linear elastic material, and a system of Maxwell's equations was used to emulate the pulsed electromagnetic field to achieve the dynamic simulation of the robot's motion.

The second step is the simulation of the pulsed magnetic field, which is a transient electromagnetic field. This is constructed by solving the equivalent equations of the Maxwell's as follows:

$$\nabla \times \mathbf{H} = \mathbf{J} \quad (3)$$

$$\mathbf{B} = \nabla \times \mathbf{A} \quad (4)$$

$$\mathbf{J} = \sigma \mathbf{E} + \sigma \mathbf{v} \times \mathbf{B} + \mathbf{J}_e \quad (5)$$

$$\mathbf{E} = -\frac{\partial \mathbf{A}}{\partial t} \quad (6)$$

In Eq. (3), ∇ is the Hamiltonian operator, \mathbf{H} denotes the magnetic field strength vector and \mathbf{J} denotes the current density vector; in Eq. (4), \mathbf{B} denotes the magnetic induction strength vector and the relationship between \mathbf{B} and \mathbf{H} is given by $\mathbf{B} = \mu_0 \mu_r \mathbf{H}$, where μ_0 denotes the vacuum permeability, μ_r denotes the relative permeability of the magnetic medium and \mathbf{A} is the vector magnetic potential; in equation (5), \mathbf{E} denotes the electric field strength vector, σ denotes the electrical conductivity. \mathbf{v} denotes the velocity vector, \mathbf{J}_e denotes the external current density and t is time [38–41].

The third step is the flow-solid coupling operation, where there is solid deformation of the robot and fluid motion of the bile in the gallbladder during motion of the robot. We describe this physical process with flow-solid coupling, taking a weakly compressible flowing fluid as the model and solving for the motion of the fluid through the Navier-Stokes equations (N-S equations) as follows:

$$\rho \left(\frac{\partial \mathbf{u}}{\partial t} + \mathbf{u} \cdot \nabla \mathbf{u} \right) = -\nabla p + \nabla \cdot (\mu (\nabla \mathbf{u} + (\nabla \mathbf{u})^T)) - \frac{2}{3} \mu (\nabla \mathbf{u}) \mathbf{I} + \mathbf{F} \quad (7)$$

In Eq. (7), ρ represents the fluid density, \mathbf{u} represents the fluid velocity, p is the fluid pressure, μ is the fluid dynamic viscosity, \mathbf{F}

represents the external force on the fluid, \mathbf{I} represents the turbulence intensity and t represents the time. The deformation of the equation according to the actual simulation requirements is obtained as:

$$\rho_1 \frac{\partial \mathbf{u}_{\text{fluid}}}{\partial t} + \rho(\mathbf{u}_{\text{fluid}} \cdot \nabla) \mathbf{u}_{\text{fluid}} = \nabla \cdot [-\rho \mathbf{I} + \mathbf{K}] + \mathbf{F} \quad (8)$$

$$\frac{\partial \rho}{\partial t} + \nabla \cdot (\rho_1 \mathbf{u}_{\text{fluid}}) = 0 \quad (9)$$

The Eq. (8), ρ_1 denotes the fluid density, $\mathbf{u}_{\text{fluid}}$ denotes the fluid velocity and \mathbf{K} denotes the time-averaged kinetic energy of the fluid, which is expressed as:

$$\mathbf{K} = (\mu + \mu_T)(\nabla \mathbf{u}_{\text{fluid}} + (\nabla \mathbf{u}_{\text{fluid}})^T) - \frac{2}{3}(\mu + \mu_T)(\nabla \mathbf{u}_{\text{fluid}}) \mathbf{I} - \frac{2}{3} \rho k \mathbf{I} \quad (10)$$

In Eq. (10), k denotes the turbulent kinetic energy, $\mu_T = \rho C_\mu \frac{k^2}{\varepsilon}$, C_μ is an empirical constant in turbulence models with a value of approximately 0.09 and ε denotes the turbulent dissipation rate.

According to Newton's second law, the internal stresses of a robot must be in balance with the external and inertial forces to which it is subjected. We deform the momentum balance equation to describe the robot's motion as follows:

$$\rho_2 \frac{\partial^2 \mathbf{u}_{\text{solid}}}{\partial t^2} = \mathbf{f}_v + \nabla_x \cdot \sigma \quad (11)$$

Eq. (11), ρ_2 denotes the density of the robot, $\mathbf{u}_{\text{solid}}$ represents the speed of the robot, t represents time, \mathbf{f}_v is the volume force, which represents the force per unit volume of deformation that occurs, and σ expresses the Corsi stress tensor.

Through the dynamic simulation, we derive physical indicators such as the variation of the pulsed magnetic field, the dynamic fluid flow velocity and fluid pressure, and the parametric equivalent force (Von Mises Stress) of the robot.

Experiments on a robotic lithotripsy system

We acquired a gallstone and performed the first lithotripsy experiment. The gallstone weight was 0.64 g (Supplementary Fig. S16b) and the diameter was approximately 12 mm (Supplementary Fig. S16a). It was placed in a gallbladder model with three robots and water. The position of the gallbladder model was fixed in the same position as during the movement test. The pulsed magnetic field strength was 0.3 T and the frequency was 80 min⁻¹. The pulsed magnetic therapy instrument was switched on for the lithotripsy experiment, and the stone was crushed. After that, the residue was poured out and dried naturally (Supplementary Fig. S16c).

In order to perform a comparative experiment between the robotic crushing of a gallstone and drug dissolution of a gallstone, we acquired two gallstones from the same patient. The medicament group is used to compare the efficacy of the robot lithotripsy program, where the drug used in the medicament group is ursodeoxycholic acid. The two lithotripsy programs are non-invasive and oral methods, which are comparable. The gallstones had a mass of 0.869 g and 0.664 g, respectively, and were 10–15 mm in size (Supplementary Fig. S17a–d). The gallstones were 0.869 g for the robot group (Supplementary

Fig. S18a) and 0.664 g for the medicament group (Supplementary Fig. S18b). The drug used was ursodeoxycholic acid tablets [42], which were dissolved and added to the gallbladder model containing the gallstones by following the dosage of the drug instructions, and after 20 min for both groups (Supplementary Video S7), the treated residue was removed for weighing and photographing (Supplementary Fig. S17e–h).

To better match the results of the lithotripsy experiments to the real environment of the human gallbladder, we purchased a porcine gallbladder from the market to carry out experiments on the crushing of human gallstones. The porcine gallbladder was dissected along the edge near the bile duct with an incision diameter of 35 mm to allow the placement of human gallstones and video observation. The pig gallbladder was fastened to a 5 mm thick acrylic plate. After three robots were placed in the gallbladder, a human gallstone (maximum diameter of 1 cm and mass of 0.2 g) was additionally added. Before lithotripsy, SPECT technology was used to assess the condition of robots and gallstones, as demonstrated in Fig. 4f. The geometric center of the pig gallbladder and the geometric center of the pulsed magnetic field generator were kept aligned. The robots were actuated by a medical pulsed magnetic therapy device (magnetic flux density 0.3 T, pulse frequency 80 min⁻¹). After 30 minutes of lithotripsy, SPECT was utilized to assess the status of the robots and gallstones, as shown in Fig. 4g. Finally, the robot and gallstone residues were removed, as shown in Fig. 4d.

Measurement of the smallest diameter of the robot through the pipe

The smallest tube diameter that the robot could pass through was investigated using a soft conical tube which was 3D printed in a silicone material (Supplementary Fig. S3a). A rectangular magnet (76 mm × 56 mm × 31 mm) was used to guide the robot into the conical tube at a distance of 1 cm from the tube until the robot was stuck in the conical tube, and the inner diameter of the conical tube at the furthest point reached by the robot was determined. It was found that the robot was able to pass through a minimum diameter of 4.85 mm, owing to the elasticity of the robot and the conical tube material.

Biological assessment and analysis of tissue sections

Gallbladder tissue (Supplementary Fig. S20c) was taken from the upper part of the gallbladder (the part that has not impinged during lithotripsy) and the bottom part of the gallbladder (the part that is repeatedly impinged during lithotripsy) and fixed in fixative solution (4% Paraformaldehyde Fix Solution) for 24 h. After trimming, they were dehydrated and then immersed in melted paraffin wax. The wax-soaked tissue was embedded in the embedding machine after the tissue had been immersed in paraffin and cooled to -20 °C. The sections were prepared using a paraffin slicer at 4 μm, unfolded in warm water at 40 °C, baked in an oven at 60 °C and removed. The sections were washed and dewaxed using xylene, anhydrous ethanol, 75% alcohol and deionised water in sequence. The sections were stained with Hematoxylin solution (C₁₆H₁₄O₆) and Eosin dye (C₂₀H₆Br₄Na₂O₅). They were then soaked in anhydrous ethanol and xylene for 5 min to complete the dehydration, fol-

lowed by sealing with neutral gum for microscopic observation and image acquisition.

Characterization and measurements

The equipment utilized in this work was a Nikon optical microscope (Nikon LV100ND) and imaging system (Nikon DS-Ri2), the software NASE Engineer for photography and measurements, and a 3D profiler (BRUKER ContourX-500) to characterize the morphological features of the spiny skin. A field-emission scanning electron microscope (FEI Nova Nano SEM 450) was used to observe the morphological features of the magnetic spiny skin and gallstones.

The medical pulsed magnetic therapy device (MC-B-II) for actuating the robots was purchased from Langfang Tianyue Medical Instrument Co. Ltd. The magnetic field generator is pancake-shaped, 152.5 mm in diameter and 35.5 mm thick, capable of generating an average magnetic pulse intensity of 0.1 T, 0.15 T, and 0.3 T. The pulse frequency can be adjusted to 20, 30, 40, 50, 60, 70, and 80 times per minute.

High-speed camera (2F04) for filming movements of robots was purchased from Hefei FuHuang AgileDevice Co., Ltd. The physical morphology of gallstones and robots in the porcine gallbladder was characterized with single-photon emission computed tomography (Triumph X-SPECT/X-OCT) system. The instruments for tissue section analysis were the dehydrator (Donatello) from DIAPATH, the embedding machine (JB-P5) from Wuhan Junjie Electronics Co. Ltd., a Pathology Microtome (RM2016) from Shanghai Leica Co., Ltd, a dyeing machine (Giotto) from DIAPATH, a Nikon Corporation Upright optical microscope (Nikon Eclipse E100) and Imaging System (Nikon DS-U3). The software used for the finite element simulations in this work is COMSOL Multiphysics 5.4.

CRediT authorship contribution statement

Lin Xu: Data curation, Investigation, Formal analysis, Methodology, Visualization, Writing - review & editing. **Heting Wu:** Data curation, Investigation, Formal analysis, Methodology, Software, Visualization, Resources, Writing - original draft. **Weiqi Qian:** Formal analysis, Visualization, Writing - review & editing. **Yang Wang:** Formal analysis, Writing - review & editing. **Chris R. Bowen:** Validation, Writing - review & editing. **Zhong Lin Wang:** Conceptualization, Funding acquisition, Resources, Supervision, Writing - review & editing. **Ya Yang:** Conceptualization, Formal analysis, Funding acquisition, Resources, Supervision, Visualization, Writing - review & editing.

Declaration of Competing Interest

The authors declare that they have no known competing financial interests or personal relationships that could have appeared to influence the work reported in this paper.

Acknowledgements

This work was supported by the National Key R&D Project from the Minister of Science and Technology in China (Grant No. 2021YFA1201604), the National Natural Science Foundation of China (Grant No. 52072041), the Beijing Natural Science Foundation (Grant No. JQ21007), and the University of Chinese Academy of Sciences (Grant No. Y8540XX2D2).

Appendix A. Supplementary data

Supplementary data to this article can be found online at <https://doi.org/10.1016/j.mattod.2022.04.012>.

References

- [1] F. Lammert et al., *Nat. Rev. Dis. Primers* 2 (2016) 16024.
- [2] A.H. van Dijk et al., *Lancet* 393 (2019) 2322–2330.
- [3] D.E. Sanford, *Surg. Clin. North Am.* 99 (2019) 245–258.
- [4] P. Portincasa et al., *Expert. Rev. Gastroenterol. Hepatol.* 10 (2016) 93–112.
- [5] M. Radunovic et al., *Open Access Maced. J. Med. Sci.* 4 (2016) 641–646.
- [6] D.M. Shabanzadeh et al., *Int. J. Public Health* 62 (2017) 353–360.
- [7] G. Sandblom et al., *HPB* 17 (2015) 239–243.
- [8] L. Pan et al., *Ann. Surg.* 268 (2018) 247–253.
- [9] D.A. Nicholson et al., *Br. J. Surg.* 79 (1992) 811–814.
- [10] S. Amplatz et al., *Dig. Liver Dis.* 39 (2007) 267–272.
- [11] H. Lu et al., *Nat. Commun.* 9 (2018) 3944.
- [12] J.C. Norton et al., *Sci. Robot.* 4 (2019) eaav7725.
- [13] H. Feng et al., *Int. J. Med. Robot.* 14 (2018) e1904.
- [14] J. Kang, et al., *Sci. Robot.* 2 (2017), eaan2634.
- [15] M. Cianchetti et al., *Nat. Rev. Mater.* 3 (2018) 143–153.
- [16] Y. Kim et al., *Sci. Robot.* 4 (2019) eaax7329.
- [17] C. Li et al., *Sci. Robot.* 5 (2020) eabb9822.
- [18] M. Ilami et al., *Adv. Mater.* 33 (2020) e2003139.
- [19] M.Z. Miskin et al., *Nature* 584 (2020) 557–561.
- [20] J. Li et al., *Sci. Robot.* 3 (2018) eaat8829.
- [21] Y. Wang et al., *Nano Energy* 63 (2019) 103810.
- [22] T.M. Jang et al., *Sci. Adv.* 6 (2020) eabc9675.
- [23] X. Yang et al., *Sci. Robot.* 5 (2020) eabc8191.
- [24] W. Hu et al., *Nature* 554 (2018) 81–85.
- [25] T. Xu et al., *Sci. Robot.* 4 (2019) eaav4494.
- [26] J. Li et al., *Sci. Robot.* 2 (2017) eaam6431.
- [27] J. Liu et al., *Adv. Mater.* 32 (2020) e1908008.
- [28] E.R. Aurand et al., *Adv. Funct. Mater.* 28 (2018) 1700550.
- [29] M.P. Wolf et al., *Prog. Polym. Sci.* 83 (2018) 97–134.
- [30] G. Reshmi et al., *Int. J. Pharm.* 365 (2009) 131–135.
- [31] V.N.T. Le et al., *Med. Phys.* 43 (2016) 650–663.
- [32] J.W. Martin et al., *Nat. Mach. Intell.* 2 (2020) 595–606.
- [33] N. Ebrahimi et al., *Adv. Funct. Mater.* 31 (2020) 2005137.
- [34] A. Mousa, et al., Self-Driving 3-legged Crawling Prototype Capsule Robot with Orientation Controlled by External Magnetic Field, in: 2018 WRC Symposium on Advanced Robotics and Automation (WRC SARA), IEEE, 2018, pp. 243–248
- [35] S. Ghosh, A. Ghosh, *Sci. Robot.* 3 (2018) eaaq0076.
- [36] S. Kocman et al., Induction motor modeling using COMSOL multiphysics, in: in: 2016 17th International Scientific Conference on Electric Power Engineering (EPE), 2016, pp. 1–5.
- [37] G. Li et al., *Nature* 591 (2021) 66–71.
- [38] D. Shah et al., *Adv. Mater.* 33 (2020) e2002882.
- [39] X. Zhang et al., *IEEE Trans. Instrum. Meas.* 68 (2019) 680–687.
- [40] S. Ge, G.M. Whitesides, *Anal. Chem.* 90 (2018) 12239–12245.
- [41] C. Di Natali et al., *IEEE Trans. Robot.* 32 (2016) 327–338.
- [42] S.H. Lee et al., *JAMA Surg.* 155 (2020) 703–711.